

NASA TECHNICAL NOTE



NASA TN D-6616

2.1

NASA TN D-6616

**LOAN COPY: RET
AFWL (DO
KIRTLAND AFE**



**CONCEPTUAL DESIGN AND ANALYSIS
OF AN INFRARED HORIZON SENSOR
WITH COMPENSATION
FOR ATMOSPHERIC VARIABILITY**

*by Antony Jalink, Jr., Richard E. Davis,
and John A. Dodgen*

*Langley Research Center
Hampton, Va. 23365*



0133213

1. Report No. NASA TN D-6616		2. Government Accession No.		3. Recipient's Catalog No.	
4. Title and Subtitle CONCEPTUAL DESIGN AND ANALYSIS OF AN INFRARED HORIZON SENSOR WITH COMPENSATION FOR ATMOSPHERIC VARIABILITY				5. Report Date February 1972	
				6. Performing Organization Code	
7. Author(s) Antony Jalink, Jr., Richard E. Davis, and John A. Dodgen				8. Performing Organization Report No. L-8013	
9. Performing Organization Name and Address NASA Langley Research Center Hampton, Va. 23365				10. Work Unit No. 115-17-07-01	
				11. Contract or Grant No.	
12. Sponsoring Agency Name and Address National Aeronautics and Space Administration Washington, D.C. 20546				13. Type of Report and Period Covered Technical Note	
				14. Sponsoring Agency Code	
15. Supplementary Notes					
16. Abstract A horizon detection logic, based on a ratio-of-integrated-radiance concept, which detects the earth's horizon at a relatively stable height under all geographic and meteorological conditions has been evaluated by computer simulation on a body of synthesized radiance profiles. An error-sensitivity analysis of the concept was performed, and optimum design parameter values for a sensor were determined. A conceptual design for an improved 15- μ m sensor based on this analysis is discussed.					
17. Key Words (Suggested by Author(s)) Infrared horizon sensing Limb radiance Infrared radiometer conceptual design Spacecraft attitude determination Carbon dioxide 15- μ m limb				18. Distribution Statement Unclassified - Unlimited	
19. Security Classif. (of this report) Unclassified		20. Security Classif. (of this page) Unclassified		21. No. of Pages 32	
				22. Price* \$3.00	

CONCEPTUAL DESIGN AND ANALYSIS OF
AN INFRARED HORIZON SENSOR WITH COMPENSATION
FOR ATMOSPHERIC VARIABILITY

By Antony Jalink, Jr., Richard E. Davis,
and John A. Dodgen
Langley Research Center

SUMMARY

A horizon detection logic, which locates the earth's infrared CO₂ horizon at a relatively stable height regardless of atmospheric variations, has been developed. A digital computer simulation study was used to optimize sensor system parameters for maximum stability of the located horizon.

The simulation study used a body of synthesized radiance profiles describing eight synoptic situations during the year 1964-65 plus the Novembers of 1965 and 1966. In all, 462 distinct, realistic radiance profiles were employed in the statistical evaluations.

This simulation was also used to determine the sensitivity of the detection logic, or locator, to a number of error sources including changes in the horizon itself and uncertainties in mission and horizon sensor parameters.

The simulation was performed to determine the performance of a single sensor head; therefore, the attitude accuracy with respect to the local vertical predicted by these studies is conservative when compared with that predicted for an operational attitude determination subsystem employing several such sensor heads.

The standard deviation (1σ) in located horizon tangent height caused by phenomenological horizon noise alone was shown to be 0.798 km; however, the sensor uncertainty increased to 1.14 km (1σ) when all error sources were considered. A conceptual horizon sensor instrument which uses a compact optical system, immersed bolometer detectors, and simple electronic circuitry was shown to have performance commensurate with this accuracy.

INTRODUCTION

A simple method to determine spacecraft attitude in earth orbit is to sense the atmospheric radiation gradient of the earth's horizon. Of course, the accuracy of this method depends strongly on the stability of the located radiation gradient with respect to

the solid earth. For this reason, the choice of the spectral band used to sense the gradient is important. More than a decade of experiments and analytical studies points to the CO₂ absorption band centered about 15 μ m as optimum for horizon sensing. (See refs. 1, 2, and 3.) A number of detection-logic concepts for 15- μ m horizon sensors have been studied previously. (See refs. 4, 5, and 6.) Present knowledge of the earth's infrared horizon can provide spacecraft attitude information to an accuracy equivalent to less than 1 km at the horizon (equivalent to an angle of 0.022° for a 500-km orbit) if a compensation or normalization technique to suppress latitude and seasonal effects is used. The range of variability to be expected in the earth's 15- μ m limb is discussed later in this report.

This paper presents a detection logic, or locator, which will detect the horizon at a relatively stable height regardless of the deterministic variations of latitude and season and which can be implemented in a simple flight instrument. The paper covers two areas of study: First, the computer simulation and parameter optimization of the locator is discussed, and second, the design of a flight sensor which incorporates the results of the optimization in a reliable instrument is presented.

SYMBOLS

D	effective diameter of optical system aperture, cm
D*	detectivity of detectors, cm-Hz ^{1/2} /W
f	frequency, Hz
f/	speed of optical system, dimensionless
G(j ω)	transfer function, dimensionless
h	tangent height, km
h _L	tangent height located by the logic, or "located" tangent height, km
\bar{h}_L	mean located tangent height, km
h _{L,max}	maximum located tangent height, km
h _{L,min}	minimum located tangent height, km

h_1	limit of integration on leading field of view, km
h_1'	limit of integration on lagging field of view, km
K	midband gain of transfer function, dimensionless
N	radiance, W/m ² -sr
NER	noise equivalent radiance, W/m ² -sr
n	random number, dimensionless
\mathcal{N}	integrated radiance, W-km/m ² -sr (see eq. (1))
R	gain ratio, dimensionless (see eq. (2))
t_s	time during which fields of view sweep across a resolution element, seconds
X_i	i th source of error, units vary (see eq. (7))
α	angle of skew, deg
Δf	noise equivalent bandwidth, Hz
Δh	separation of fields of view, km (see fig. 2)
ΔX_i	expected value of error for X_i , units vary
$\Delta\Omega$	solid-angle field of view, sr
$\delta_{o,e}$	radiometric efficiency of instrument optics and electronics, dimensionless
$\delta\bar{h}_{L,i}$	i th change in mean located tangent height, km
ϵ_L	vertical tangent-height difference, km
σ	standard deviation, km
$\sigma(h_L)$	standard deviation of located tangent height, km

σ^2 variance, km^2

$\sigma^2(h_L)$ variance of located tangent height, km^2

τ_{det} detector time constant, sec

HORIZON SENSING

To determine the attitude of a spacecraft in near-earth orbit, an apparent horizon formed by the thermal emission from the earth's atmosphere can be sensed against the effective temperature of interstellar space (3.1 K). Figure 1 illustrates the horizon-sensing geometry of a spacecraft with four sensor heads whose fields of view are equally

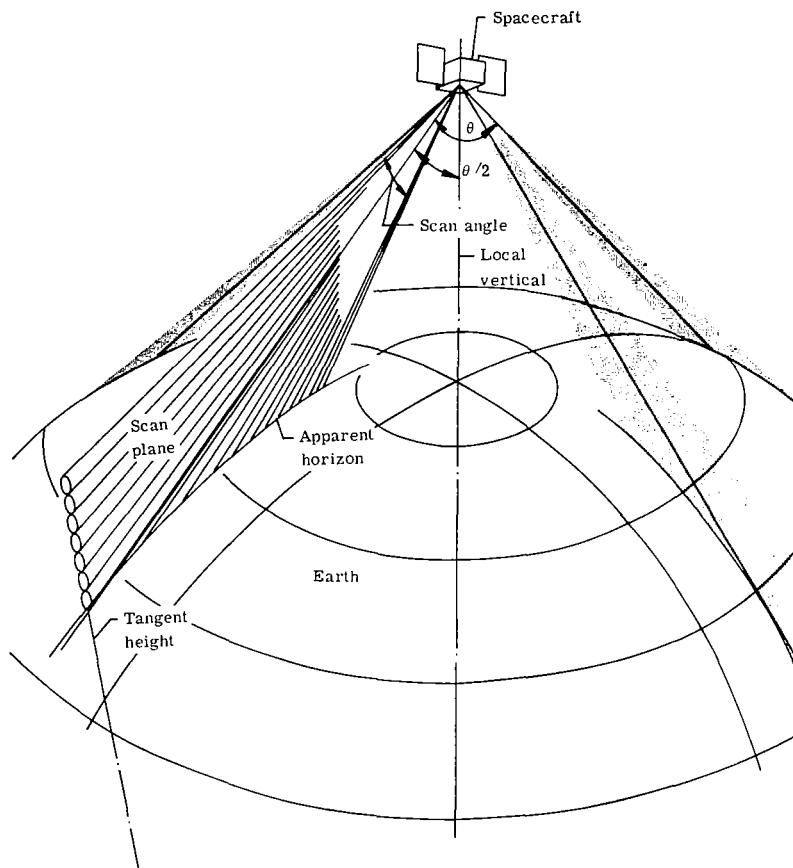


Figure 1.- Horizon-sensing geometry.

spaced about the earth. For the horizon-sensing technique of interest in this paper, each sensor-head field of view is continuously scanned from space to earth and back again. Each instantaneous line of sight contains a point which is closest to the solid earth; the vertical height of this point above the earth is termed "tangent height."

The sensor heads use a detection logic to define the location of the apparent thermal horizon at a relatively constant and fixed tangent height above the earth. The detection logic senses the point where the sensor-head field of view crosses through the apparent horizon. Once the horizon is defined, the spacecraft attitude (angle with respect to local vertical) can be derived by bisecting the angle θ between the lines of sight of opposing sensor heads. The angle to the local vertical ($\theta/2$) can also be determined geometrically by using a single sensor line of sight when the spacecraft altitude and the tangent height of the apparent horizon are known.

The accuracy of the attitude determination depends directly on the height stability of the apparent horizon. A detection logic capable of defining a stable infrared horizon is introduced in the following section.

DETECTION LOGIC: THE RATIO-OF-INTEGRATED-RADIANCE LOCATOR

The ratio-of-integrated-radiance locator detects the altitude at which a fixed ratio exists between two radiance integrals each having different limits of integration. The integrals have the general form

$$N = \int_{h_0}^{h_1} N(h)dh \quad (1)$$

where h_0 and h_1 are the tangent heights between which the integration is carried out, and $N(h)$ is the radiance of the earth's atmosphere as related to the tangent height. Both integrals that make up the ratio have space, that is, the tangent height where $N(h)$ is zero, as their lower limit of integration. The upper limit of integration is a different tangent height for each integral. The locator is satisfied when one integral is a pre-chosen multiple of the other, as expressed by

$$\int_{\infty}^{h_1} N(h)dh = R \int_{\infty}^{h'_1} N(h)dh \quad (2)$$

The value of the constant of multiplication R , as well as the values of h_1 and h'_1 , is chosen so that maximum stability of the locator is obtained. Figure 2 is a schematic representation of the manner in which the two integrals of equation (2) can be generated in a sensor. The integrals are the energy received by the two fields of view (abbreviated FOV) which are scanned simultaneously from space to earth. Since the two fields of view move together, $N(h)$ is the same function in both integrals; therefore, choosing the separation $\Delta h = h_1 - h'_1$ is synonymous with choosing the location of h_1 and h'_1 . When the quantities on each side of the equation become identical, the horizon is located; then

$$\int_{\infty}^{h_1} N(h)dh - R \int_{\infty}^{h'_1} N(h)dh = 0 \quad (3)$$

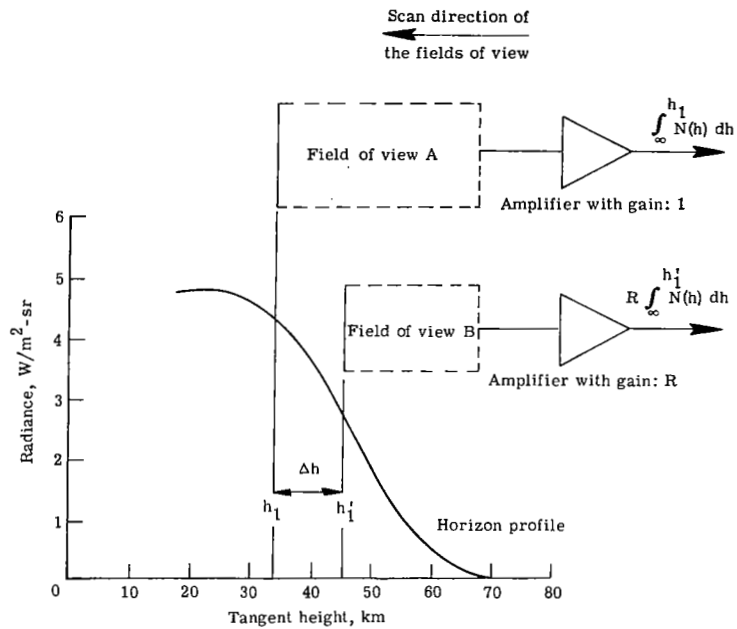


Figure 2.- Schematic showing how the radiance integrals are obtained.

A schematic representation of the principle of locator operation is shown in figure 3. The solid lines, curves 1 and 2, show the value of each integral as a function of tangent height h for winter conditions, and the dashed lines, curves 3 and 4, are pro-

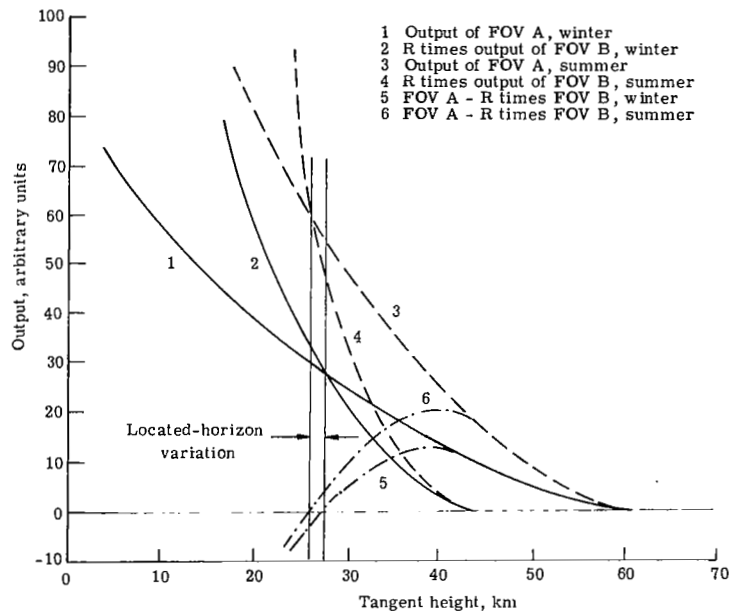


Figure 3.- Principle of locator operation (for winter and summer conditions).

duced for summer conditions. The dash-dot lines, curves 5 and 6, represent the left-hand side of equation (3) – one for winter conditions, the other for summer conditions. The horizon is located where the dash-dot line, for example curve 5, crosses the

zero-output line. For accurate horizon sensing, the located-horizon variation must be minimized. The values of the field-of-view leading-edge separation $h_1 - h'_1$ and of effective gain R should be chosen such that these latter curves cross the zero-output line at a steep angle and, as much as possible, at the same tangent height for the most stable and accurate horizon location. The following section summarizes the computer studies performed to simulate the locator performance and to determine the optimum values of $h_1 - h'_1$ and R .

ANALYTICAL SIMULATION OF THE LOCATOR

The performance of the detection logic under a wide range of atmospheric conditions was simulated by using a body of meteorological data and some analytical techniques developed previously and described in references 6 to 10. For the convenience of the reader, a description of the data and the analysis techniques is given herein.

Meteorological Data and Radiance Profiles

As shown in references 2, 3, 7, and 8, the shape of the earth's limb in the 15- μ m CO₂ band changes as the vertical temperature and pressure profiles vary within the atmosphere. Since these physical quantities tend to change in a deterministic way with season and latitude, the radiance profiles should also. However, synoptic meteorological situations (e.g., highs, lows, stratospheric warmings) tend to weaken this determinism and therefore introduce a random component.

The horizon-sensor designer must consider the effects of profile changes caused by these atmospheric conditions, which are called "phenomenological noise." This error source can be evaluated by simulating the operation of a horizon detection logic on a number of radiance profiles representing the expected seasonal and synoptic changes. In this way the performance of the locator can be determined as a mean located tangent height with an accompanying variance σ^2 . The parameters of the detection logic can thus be optimized to achieve a minimum variance, and the effects of instrumental parameters can be determined.

The meteorological data base used in this study is described in reference 8, and consisted of 1085 horizon radiance profiles generated from real and synthesized meteorological data obtained from rawinsonde balloons, Meteorological Rocket Network (MRN) soundings, and empirical extrapolation methods from a previous study (ref. 9). This body of data was believed to be the best available for analysis because it is the only body of data which uses real meteorological data in the generation of radiance profiles and it simulates, by eight synoptic situations, an entire year of data from 0° to 90° latitude over North America. Thus, it has provided data for the most realistic simulation of the earth's

infrared horizon as it varies with latitude, longitude, season, and synoptic situation. The radiance profiles were computed by the CORPS (Comprehensive Radiance Profile Synthesizer) program (ref. 7) for the 14.0- to 16.3- μm (715 to 615 cm^{-1}) spectral interval.

Of the 1085 radiance profiles mentioned, 448 represent eight synoptic situations each having 56 data points spread over North America from 0° to 90° N and between 60° and 160° W for the period March 1964 through February 1965. Of these, 350 profiles representative of the seasonal and synoptic variations were used for this simulation. Within this 350-profile set, anomalies were noted for the November 1964 profiles. Therefore, meteorological data for the Novembers of 1965 and 1966 were assembled into a form suitable for analysis. It was found that the November 1964 data represent a stratospheric warming condition, and the other two Novembers represent more typical seasonal conditions. Each of the additional Novembers had 56 data points; thus, 462 profiles, in all, were used in analyzing and optimizing the locator concept.

The radiances for the horizon profiles were computed in tangent-height regions with varying resolution, that is, low resolution where radiance changes slowly and high resolution where radiance changes rapidly with tangent height, as follows:

<u>Tangent-height region, km</u>	<u>Resolution, km</u>
-30 to -10	5
-10 to 0	2
0 to 50	1
50 to 60	2
60 to 80	5

Basic Elements

To expedite analysis of locator concepts over a range of conditions, certain properties called "basic elements" of each radiance profile were determined as related to tangent height and then compiled into a reference library, as described in reference 6. The six basic elements are

- (1) Radiance
- (2) Integral of radiance over tangent height from 80 km downward along the radiance profile
- (3) Radiance normalized to peak radiance of the profile
- (4) Integral of radiance, normalized to peak radiance of the profile
- (5) Derivative of radiance with respect to tangent height
- (6) Second derivative of radiance with respect to tangent height

All the basic elements are computed with the same resolution used for the radiance profiles.

Locator Processor Program

The analysis techniques and computer program described in reference 6 were used to simulate the operation of the locator concept on radiance profiles synthesized from the selected body of atmospheric data. In summary, the computer program uses the appropriate basic elements data to determine the located altitude for a specific radiance profile and locator concept. A number of radiance profiles representing a range of atmospheric conditions are analyzed; then the performance of the horizon sensor is described by the following parameters:

- (1) Mean located tangent height \bar{h}_L
- (2) Maximum located tangent height $h_{L,max}$
- (3) Minimum located tangent height $h_{L,min}$
- (4) Variance of located tangent height $\sigma^2(h_L)$
- (5) Standard deviation of located tangent height $\sigma(h_L)$

This program was used as the starting point for the mathematical formulation and testing of the new locator described in this paper. The program was improved to allow simulation of the effects of important sensor-related noise sources.

Simulation of the Locator by Numerical Techniques

The phenomenological operation of the recommended horizon detection logic is shown in figure 4. The integrated radiances from the two spatially related fields of view are denoted by the two different hatchings.

In the mechanizations of this locator technique (to be discussed in this report), the signals corresponding to the two integrated radiances are processed electronically. The radiometric output of the sensor is proportional to the difference between the larger of the integrated radiances and R times the smaller. The output \mathcal{N}_L as found from equation (3) is

$$\mathcal{N}_L = \int_{\infty}^{h_1} N(h)dh - R \int_{\infty}^{h'_1} N(h)dh \quad (4)$$

When $\mathcal{N}_L = 0$, the locator is satisfied. The altitude h_1 for which this occurs is denoted h_L , hereinafter called the located tangent height found by the sensor. Since the basic data are available only at discrete tangent-height intervals, a nonlinear interpolation routine was developed to determine the exact value of the located tangent height.

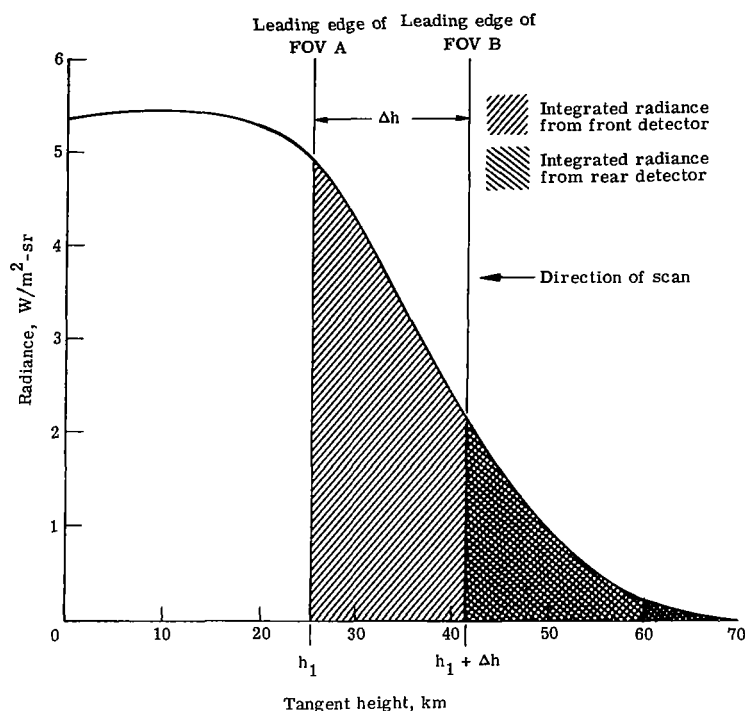


Figure 4.- Operation of ratio-of-integrated radiance locator on a computer-generated profile.

Determination of Optimal Sensor Parameters

To select the optimal values for the sensor parameters R and Δh , the following three-step procedure was used:

- (1) The range of R and Δh combinations providing the lowest standard deviation was found by using climatological profiles representing the mean and extreme conditions to be encountered.
- (2) The best R and Δh combination was then selected by using the 350-profile subset, which provided a measure of the performance over seasonal, geographical, and synoptic conditions.
- (3) The selected locator parameters were then subjected to additional profile subsets representing anomalous conditions and were perturbed to evaluate the effects of instrumental errors or uncertainties.

To accomplish the first step, the arctic summer and cold arctic winter model atmospheres for 60° N latitude were chosen from reference 7 to represent the extremes, and radiance profiles for these and the 1962 standard atmosphere (ref. 11) are shown in figure 5. From these data it was found that the optimum combinations of R and Δh would lie in the range $3.8 \leq R \leq 4.7$ and $16 \leq \Delta h \leq 18$ km. For example, R and Δh combinations with low variances were found to be 3.8 and 17 km, 4.05 and 17 km, 4.3 and 18 km, and 4.7 and 18 km.

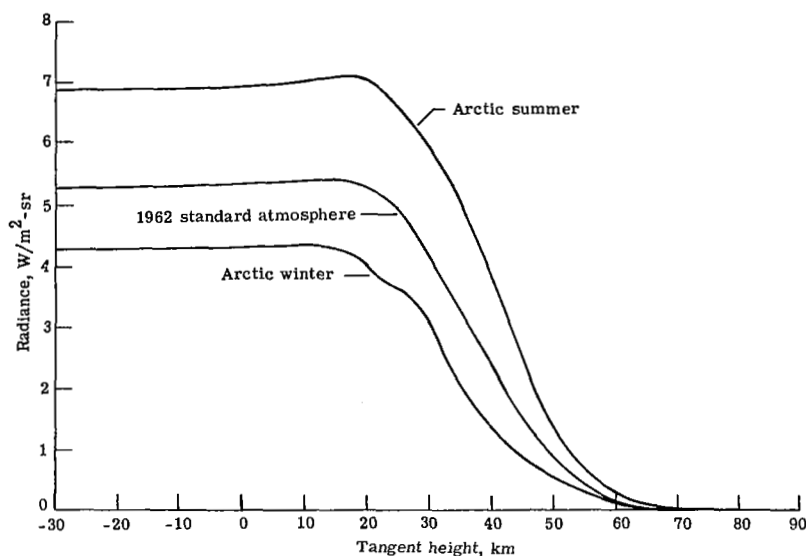


Figure 5.- Horizon radiance for 1962 standard atmosphere and climatological extremes in the 14.0 to 16.3- μ m band (adapted from ref. 7).

The second step was initiated on the basis of the preceding results; however, the investigated ranges for R and Δh were broadened to determine the effects of synoptic, or phenomenological, noise. Table I shows the results of running a matrix of combinations on the 350-profile subsets. (The dashes indicate combinations for which no

TABLE I.- VARIANCES OF LOCATED TANGENT HEIGHT FROM 350-PROFILE SET

R	Variance, km ² , for Δh of -				
	12 km	14 km	16 km	18 km	20 km
3.0	0.840	1.434	2.061	2.476	2.821
3.1	.910	1.257	1.918	2.358	2.669
3.2	1.090	1.097	1.769	2.251	2.570
3.3	1.322	.957	1.617	2.124	2.488
3.4	1.544	.843	1.467	2.006	2.373
3.5	1.724	.771	1.326	1.893	2.267
3.6	1.867	.751	1.186	1.764	2.169
3.7	1.963	.780	1.060	1.638	2.110
3.8	1.996	.868	.945	1.522	1.978
3.9	1.967	1.000	.845	1.408	1.888
4.0	1.867	1.141	.768	1.293	1.786
4.1	1.711	1.285	.712	1.190	1.694
4.2	1.518	1.417	.680	1.080	1.603
4.3	1.308	1.533	.674	.988	1.488
4.4	1.089	1.637	.694	.896	1.402
4.5	----	1.703	.741	.820	1.311
4.6	----	1.741	.804	.752	1.209
4.7	----	1.731	.882	.698	1.127
4.8	----	1.687	.965	.655	1.055
4.9	----	1.604	1.047	.624	.966
5.0	----	1.492	1.134	.600	.900
5.1	----	1.331	1.215	.610	.836

solutions were obtained.) Inspection shows that the best performance was obtained at $R = 5.0$ and $\Delta h = 18$ km; however, a trend of minimum variance can be seen where $R \div \Delta h \approx 0.27 \text{ km}^{-1}$ (i.e., $\frac{3.6}{14} \text{ km}^{-1}$, $\frac{4.3}{16} \text{ km}^{-1}$). There are several practical reasons for keeping both R and Δh small, including the deleterious effects of radiometric noise and optical design problems. Subsequent trade-off analyses led to the selection of $R = 4.65$ and $\Delta h = 17$ km as nominal design values. Table II shows the statistics of located tangent height as R is varied about the nominal value for $\Delta h = 17$ km, where $\sigma^2(h_L)$ and $\sigma(h_L)$ are the variance and standard deviation, respectively, and \bar{h}_L is the mean tangent height of the leading (lower) edge of field of view A (fig. 4).

TABLE II.- RESULTS OF VARYING R ABOUT THE OPTIMUM VALUE
[$\Delta h = 17$ km]

R	\bar{h}_L , km	$\sigma^2(h_L)$, km^2	$\sigma(h_L)$, km	$h_{L,\text{max}}$, km	$h_{L,\text{min}}$, km
4.05	24.040	0.962	0.981	26.759	20.810
4.15	24.556	.865	.930	27.334	21.500
4.25	25.053	.787	.887	27.874	22.211
4.35	25.541	.723	.850	28.363	22.952
4.45	26.013	.678	.824	28.839	23.670
4.55	26.473	.650	.806	29.277	24.405
4.65	26.919	.637	.798	29.701	24.968
4.75	27.351	.649	.806	30.101	25.344
4.85	27.760	.677	.823	30.479	25.744

The third step of the optimization consisted of testing the nominal design values on independent subsets of data, comprising that for Novembers 1965 and 1966, where the 4.65- and 17-km values were verified. Additional tests performed are described in the sections entitled "Error Analysis" and "Other Instrument Design Effects."

ERROR ANALYSIS

For purposes of this analysis, only those error sources which affect the performance of the locator are considered. Other error sources which are primarily instrumental in nature, such as boresight alinement and stability, and scan-angle-pickoff uncertainties, will be left to the designer of the detailed hardware.

The following error sources will be discussed in the order listed:

- (1) Instrument (radiometric) noise
- (2) Departure of satellite altitude from design goal
- (3) Skewing of the scan from the vertical

- (4) Field-of-view offset misalignment
- (5) Gain instabilities (changes in R)
- (6) Simultaneous responsivity changes in both channels

The criteria used to evaluate each error effect were the increase in variance of the located tangent height for a profile subset and the change in the mean located tangent height. The variance for an ideal sensor using this locator includes only the atmospheric, or phenomenological, noise, and each error source will cause the variance to increase from the purely phenomenological figure.

The error analysis for this report was performed for a single sensor line of sight and is therefore conservative for an operational attitude determination subsystem consisting of several sensors whose lines of sight are spaced about the local horizon. As discussed previously, the multisensor subsystem is not sensitive to changes in the average located tangent height and is less sensitive to single line-of-sight altitude changes.

Instrument Noise

In this analysis, the effects of radiometric noise introduced by the electro-optical detection subsystem were evaluated. Since the effects of phenomenological noise had been minimized when the locator parameters were selected and were known quantities, the purely phenomenological numbers were adopted as the basis for comparison.

In the computer simulation, instrument noise must be expressed in terms of instantaneous changes in the two radiance integrals corresponding to the two fields of view. The one-sigma (1σ) value of sensor random noise in terms of an equivalent change in the radiance integral is expressed by the sensor noise equivalent radiance NER multiplied by the tangent-height range subtended by the sensor FOV at the horizon. The sensor noise integral \mathcal{I} for each FOV is

$$\mathcal{I}(1\sigma) = (NER)(\text{Vertical extent of FOV}) \quad (5)$$

To simulate the random effect of the instrument noise, equation (5), which expresses the one-sigma noise value, is multiplied by a random number n obtained from a computer subprogram. To assure independence of the noise value used in the two fields of view, the subroutine is called on twice to provide independent random numbers for each FOV. The random value of sensor noise added is then

$$\mathcal{I} = n(NER)(\text{Vertical extent of FOV}) \quad (6)$$

To evaluate the effects of different amounts of radiometric noise and to determine the ultimate tolerance of the locator technique to it, several NER values were simulated. The results are shown in table III. Since the limb radiance above 80 km tangent height is assumed to be negligible for sensors of this type, the vertical extent of the FOV of

each sensor is designed so that the upper edge of the FOV is near 80 km when the lower edge is at \bar{h}_L for FOV A and at $\bar{h}_L + 17$ km for FOV B. Thus, it is concluded that NER values up to $0.15 \text{ W/m}^2\text{-sr}$ will have little effect on the performance of the locator.

TABLE III.- RESULTS OF NOISE SIMULATION OVER THE 350-PROFILE SET

NER, $\text{W/m}^2\text{-sr}$	\bar{h}_L , km	$\sigma^2(h_L)$, km^2	$\sigma(h_L)$, km
0	26.919	0.637	0.798
.05	26.828	.765	.865
.10	26.833	.814	.902
.15	26.839	.834	.913

Departure of Satellite Altitude From Design Goal

The leading edges of the two fields of view should be positioned so that for a design satellite altitude, their separation will, as closely as possible, equal the optimal value. For this simulation, the desired altitude was assumed to be 500 km. Therefore, the optimum separation of 17 km derived earlier was used. Again, the body of data used for simulation was the 350-profile set. The change in mean located tangent height as a function of departure from the desired satellite altitude is shown in figure 6. The data indicate that for a 1-km increase in satellite altitude, there is a -0.044 -km change in mean located tangent height. The behavior of the variance of the 350-profile set is shown by the dashed curve.

Skewing of the Scan From the Vertical

If the scanning motion of the sensor fields of view is not along a radius vector of the earth because of spacecraft tilt, the located tangent height is changed by two effects which tend to compensate each other.

The first effect is caused by the geometry of the situation, which in turn has two parts. Figure 7 shows that for a fixed sensor scan angle and a nominal horizon depression angle, the line of sight will generate a conical surface as the spacecraft tilts. Since the sensor output angle reference is the half-angle of this cone, the altitude indicated by the sensor and the true tangent height of the line of sight differ as a function of the skew angle. Additionally, the surface of the earth drops away in a similar but less pronounced manner. The combined height caused by these two parts is shown as ϵ_L in figure 7 for a skew angle of α . Table IV shows the vertical distances (columns (3) and (4)) as well as the combined height for various values of skew (column (5)).

The second effect skewing has on located tangent height is the change that is caused by the tilt angle of the fields of view. The FOV leading edges deviate from the horizontal

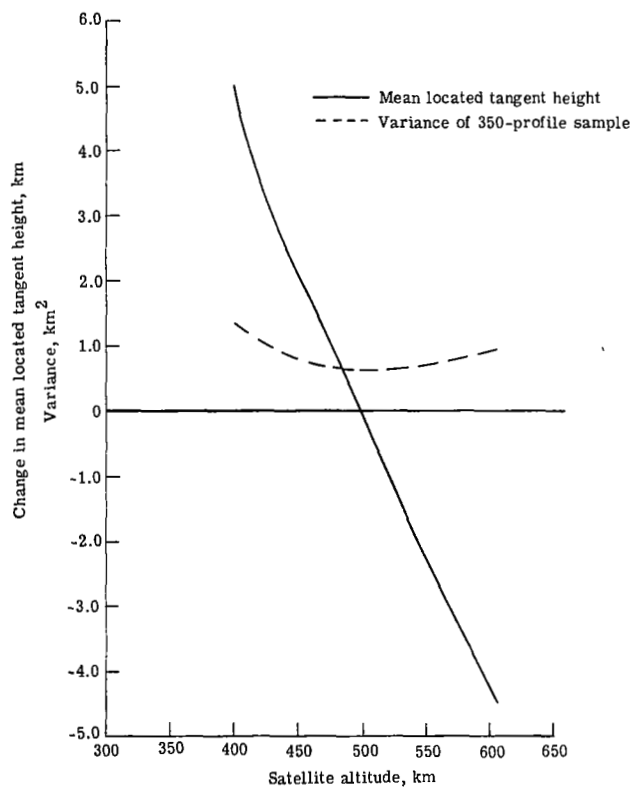


Figure 6.- Effects of change in satellite altitude on mean located tangent height and variance of locator FOV separation at horizon $\Delta h = 17$ km; gain ratio $R = 4.65$.

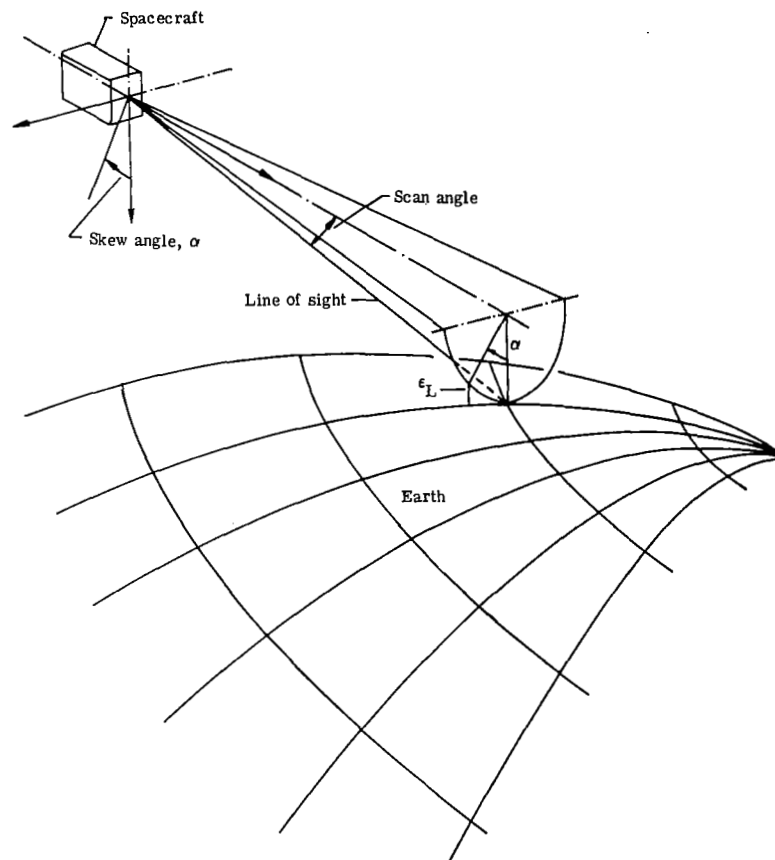


Figure 7.- Geometry of scan motion skew.

by an angle equal to the skew; this causes the sensor to locate at an increased tangent height for the fields-of-view configuration discussed elsewhere in this report. To analyze this effect, a simulation using a technique similar to that described in the section on blur circle was employed. The results of the analysis are shown in table IV (column ⑥).

The difference in tangent-height changes due to geometry and locator logic is the error in spacecraft attitude angle introduced by skewing of the scan motion. Table IV shows that this error can be minimized by proper selection of the sensor FOV horizontal width.

TABLE IV.- EFFECTS OF SKEWING FOR TWO FOV HORIZONTAL WIDTHS

① FOV horizontal width, deg	② Angle of skew, deg	③ Distance FOV rotates up, km	④ Distance earth curves down, km	⑤ Sum of columns ③ and ④, km	⑥ Increase in located tangent height, km	⑦ Error in located tangent height caused by skew (⑥ - ⑤), km
6.05	0.75	0.084	0.003	0.087	0.142	0.055
6.05	1.50	.336	.012	.348	.595	.247
6.05	3.00	1.335	.047	1.382	3.257	1.875
3.40	.75	.084	.003	.087	.042	-.045
3.40	1.50	.336	.012	.348	.133	-.215
3.40	3.00	1.342	.048	1.390	.569	-.821

Field-of-View Offset Misalignment

A misalignment in the relative boresighting of the two detectors will cause an error in Δh (fig. 4) at the horizon. Figure 8 shows the effects of large changes in Δh on the mean located tangent height \bar{h}_L for the 350-profile test set. As can be seen, a 1-km change in Δh will cause a change of approximately 2.3 km in \bar{h}_L . An estimate of the detector placement error was previously reported in reference 12 to be of the order of 5 arc seconds. For a 500-km altitude, this error corresponds to a change in Δh of only 0.14 km. This placement, therefore, would cause a change in \bar{h}_L of only 0.322 km, with negligible increase in variance.

Gain Instabilities (Changes in R)

Slight changes in R affect the locator altitude as shown in figure 9. Over the range of interest the sensitivity corresponds to a 4.2-km variation in mean located tangent height for unit change of R .

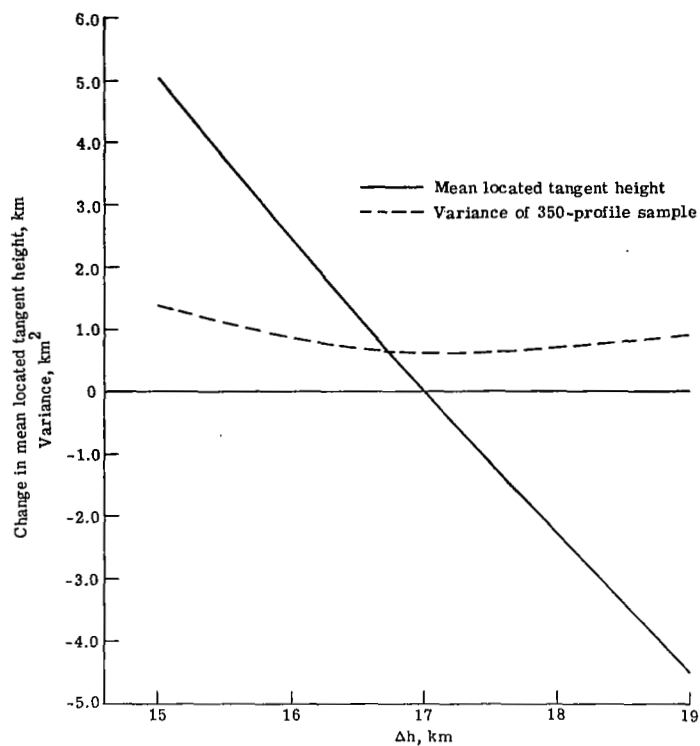


Figure 8.- Effects of changes in Δh on mean located tangent height and variance of the locator. Nominal satellite altitude, 500 km; gain ratio $R = 4.65$.

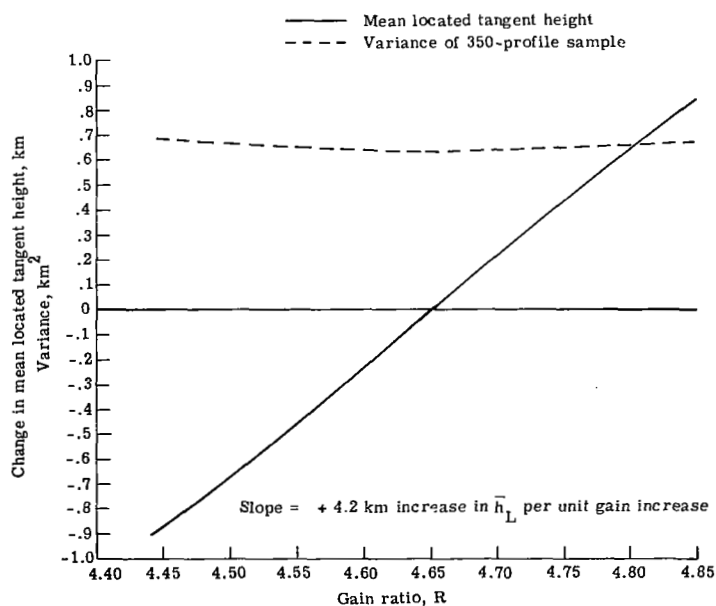


Figure 9.- Effects of gain ratio changes on mean located tangent height and variance of locator. Nominal satellite altitude, 500 km; FOV separation at horizon $\Delta h = 17$ km.

Simultaneous Responsivity Changes in Both Channels

As will be mentioned in the section entitled "Sensor Design," there are several effects which may cause the responsivity of both channels to change by the same percentage. The effect of simultaneously changing the gain over a 5-percent range from nominal was found to be negligible, as was expected.

Total Error

The magnitudes which might be expected of the various error sources just discussed are compiled in table V. Part of these magnitudes were substantiated by references 12 and 13. Also in the table are given the error sensitivities gleaned from the various figures discussed in this section and the magnitude of error in \bar{h}_L which each error source would cause.

TABLE V.- SOURCES, MAGNITUDES, SENSITIVITIES, AND EXPECTED VALUES OF ERROR IN MEAN LOCATED TANGENT HEIGHT

i	Error source, X_i	Magnitude of error, ΔX_i	Error sensitivity, $\partial \bar{h}_L / \partial X_i$	Expected value of $\delta \bar{h}_{L,i}$, km
1	Radiometric noise	0.05 W-km/m ² -sr	See table III	-0.091
2	Altitude	±25 km (ref. 13)	-0.044 km/km	±1.14
3	Skewing	±0.5°	See figure 7	+0.15
4	FOV offset	±5 arc sec (ref. 12)	+2.3 km/km	±0.32
5	Gain instability	±3%	+4.2 km/unit gain increase	±0.59
6	Simultaneous gain changes	±5%	-----	-0.001 to +0.002

If all effects are assumed to be independent, their combination for the six error effects discussed is root sum squared as follows:

$$\Delta \bar{h}_L = \left[\sum_{i=1}^6 (\delta \bar{h}_{L,i})^2 \right]^{1/2} = \left[\sum_{i=1}^6 \left(\frac{\partial \bar{h}_L}{\partial X_i} \Delta X_i \right)^2 \right]^{1/2} \quad (7)$$

where

$\Delta \bar{h}_L$ change in mean located tangent height due to all error sources considered

X_i ith cause of error

$\partial \bar{h}_L / \partial X_i$ error sensitivity of \bar{h}_L per unit change in X_i

$\delta \bar{h}_{L,i}$ ith change in mean located tangent height, km

ΔX_i expected value of error for X_i

When the six effects are combined, the rss error is 1.30 km. It should be emphasized that over 95 percent of the combined error is caused by the 25-km error assumed in satellite altitude if a circular orbit is assumed. If this error is held to 10 km, the rss error decreases to 0.82 km. This 10-km altitude error was assumed for further calculations. The rss of the 0.82-km noise figure and the 0.798-km phenomenological noise amounts to 1.14 km. In multiple-sensor-head applications the error due to satellite altitude errors does not have to be included. Indeed, it need be included only in configurations where only one horizon is crossed.

OTHER INSTRUMENT DESIGN EFFECTS

Up to this point, the analysis of the locator concept has not considered the effects of blur circle or spectral filter response. These effects are considered briefly now, not as errors, but for the insight they may give into hardware designs for this horizon sensor.

Blur-Circle Effects

In reality, the edges of both fields of view A and B do not obey the idealized step response assumed in the preceding discussion. Instead, the optical blur circle tends to smear the FOV leading edges over a finite altitude increment. In the conceptual sensor design presented in this paper, the image plane is such that field of view B is farther from the optical axis than field of view A. Thus, field of view B is subject to larger aberrations, and the effective blur circles will consequently be larger. To investigate the effects of this blurring in the presence of radiometric noise, three cases were evolved and tested over the same subset of profiles described previously. A simplified simulation of blurring, which uses a linear ramp, was employed in each case. The cases are as follows:

Case 1. - A 0.03° blur circle is introduced in each field of view. The discrete representation of the horizon described earlier makes this equivalent to what has been simulated to date.

Case 2. - A 0.08° blur circle is introduced in each field of view.

Case 3. - Because of the distortion tendency for FOV B, a blur circle of 0.2° was put in FOV B; the blur circle in FOV A was kept at 0.08° .

The behavior of the variance in located tangent height over the 350-profile set for each of these cases is shown in figure 10. Note that for the maximum noise simulated, $0.10 \text{ W/m}^2\text{-sr}$, the variance increases from 0.814 km^2 in case 1 to 0.916 km^2 in case 3. Also, the mean located tangent height increased about 0.15 km from case 1 to case 3.

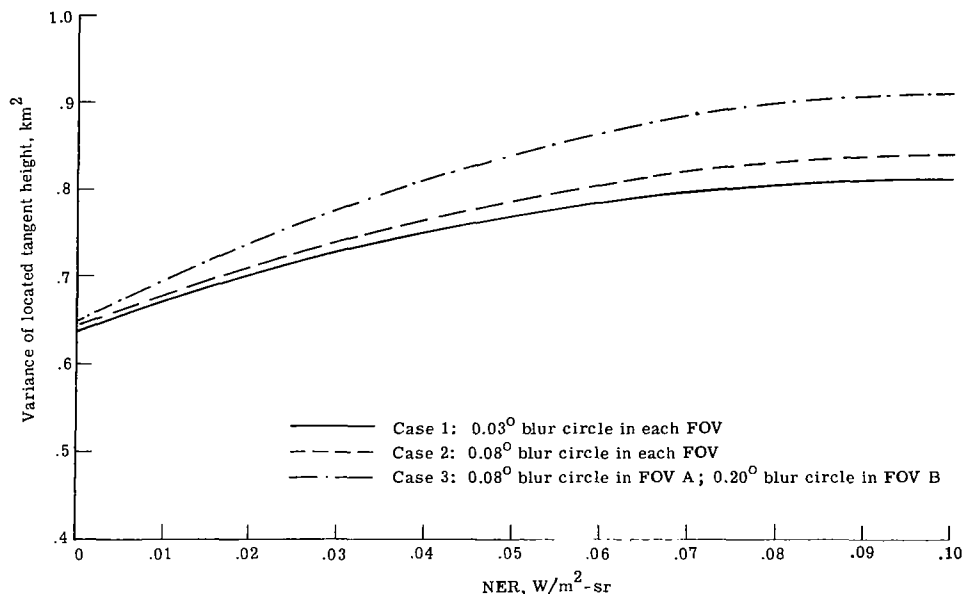


Figure 10.- Combined effects of blur circle and noise.

Spectral Filter Response Effects

In the analysis to this point, a system of 100-percent response between 14.0 and $16.3 \mu\text{m}$ (715 and 615 cm^{-1}) has been employed for maximum horizon stability as was recommended in reference 5. In practice it is impossible to fabricate such a system. To show the effects of a realistic system, the spectral response curve of an existing radiometer (shown in fig. 11) was used. For comparison, the response assumed for optimization (square between 14.0 and $16.3 \mu\text{m}$) is also shown in the figure. The results for both filters are as follows:

	$\bar{h}_L, \text{ km}$	$\sigma^2(h_L), \text{ km}^2$
Optimization filter	27.061	1.101
Real filter	29.291	0.996

It is noted that although \bar{h}_L changes 2.23 km , its variance changes little. This result is to be expected; the analysis performed in the preparation of reference 2 indicated a similar small change. Therein it was found that for each filter the ratio of the radiance through a square filter to the radiance through the actual filter in the 14.0 - to $16.3\text{-}\mu\text{m}$ band was constant to approximately 1 percent for tangent heights between 0

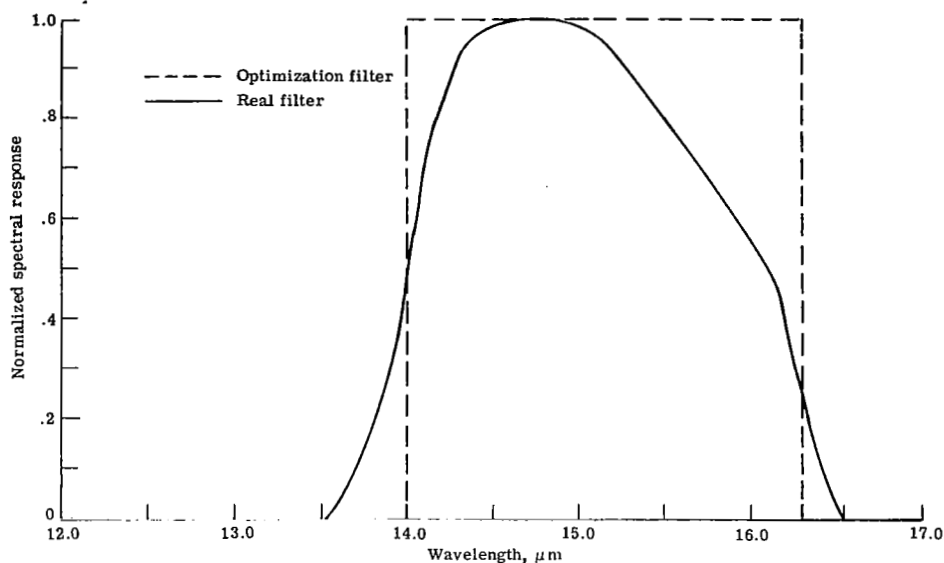


Figure 11.- Normalized spectral response of arbitrary radiometer systems simulated.

and 60 km. Since the value of the constant does depend on the filter shape, the effects of using different filters in each field of view can be important and must be considered.

It should be noted that these results are for a 125-profile subset and not for the 350-profile subset, since the simulation of spectral response effects is very time consuming with the current software for locator simulation. The particular subset chosen comprised the winter months. For this reason, the variances shown here are higher than for the 350-profile subset which included the spring and summer seasons, with their typical low variability; consequently, the variance was lower for the larger subset.

Refinements

To further improve the performance of the locator, autonomous correction schemes based on the characteristics of the sensed radiance were given limited study as a means for reducing the effect of large deterministic variations or anomalies. One of the correction algorithms investigated reduced the 1σ variability of the locator, in the absence of instrument noise, from 0.798 to 0.652 km but required considerable additional logic circuitry. This complexity was not considered necessary for most applications in view of the performance demonstrated by the basic locator.

SENSOR DESCRIPTION

The design requirements for a flight sensor which incorporates the ratio-of-integrated-radiance locator can be determined when a typical spacecraft application is considered. A further consideration is the accuracy goal of 1.5 km at the horizon, which

corresponds to an angle of 0.033° from a 500-km orbit. This accuracy requirement includes the errors introduced by both horizon variations and sensor noise.

The sensor continuously scans two fields of view of fixed relative position from space onto the earth and back to space again. The horizon is located on each down sweep so that the instantaneous "horizon angle" is available once during each scan. The spacecraft itself may exhibit in-orbit pitch, roll, and yaw motions, which require the sensor to acquire the horizon at an angle on either side of the nominal horizon direction. The total scan angle is made 5° of arc to insure that the horizon will continue to be crossed during normal spacecraft motions. Spacecraft motions are assumed to be relatively slow so that a 1-Hz sampling rate is sufficient to update spacecraft attitude. The data rate and sweep angle can be traded off to satisfy alternate mission requirements. The scanning motion can be imparted to the fields of view in two different ways: by mechanical means, such as a scan mirror, or by using a detector array in conjunction with an electronic commutator switch to eliminate moving parts. A mechanically scanned mirror was selected since the present state of the art for electronically scanned arrayed detectors does not yield as high a signal-to-noise ratio.

The sensor telescope requirements are determined by adequate signal-to-noise ratio and spatial resolution. Instrument noise should produce only negligible errors in locating the horizon as compared with variations in the horizon itself. The relationship between sensor noise equivalent radiance (i.e., the input radiance value which produces a signal-to-noise ratio of 1) and the error in located horizon tangent height it produces is shown in table III. Additionally, the sensor optical system must provide spatial resolution commensurate with the inherent accuracy of the horizon. The ratio-of-integrated-radiance locator has the advantage, in this respect, that the ratio is not changed when each integral is multiplied by the same constant. Therefore, a small amount of blur introduced by the sensor optics, which results in an almost equal gain change in each channel, has a minimum effect on locating the horizon, as was shown in the section entitled "Analytical Simulation of the Locator."

Only a detector which can operate at ambient temperature (uncooled) is considered, in the interest of simplicity, reliability, and lightness. The thermistor bolometer meets the requirements for this sensor application and has been successfully used in several space flight missions. The long-term reliability is adequate if the detector is properly selected after a 1000-hour burn-in. The performance of the sensor equipped with bolometer detectors is analyzed in detail in the following section.

SENSOR DESIGN

A schematic representation of a conceptual horizon sensor is shown in figure 12. In the vertical direction, the leading edges of the fields of view are offset a distance of

17 km at the horizon, the optimum Δh for a 500-km orbit. Also, to insure optimum performance of the locator, radiometric channel B has 4.65 times the gain of channel A.

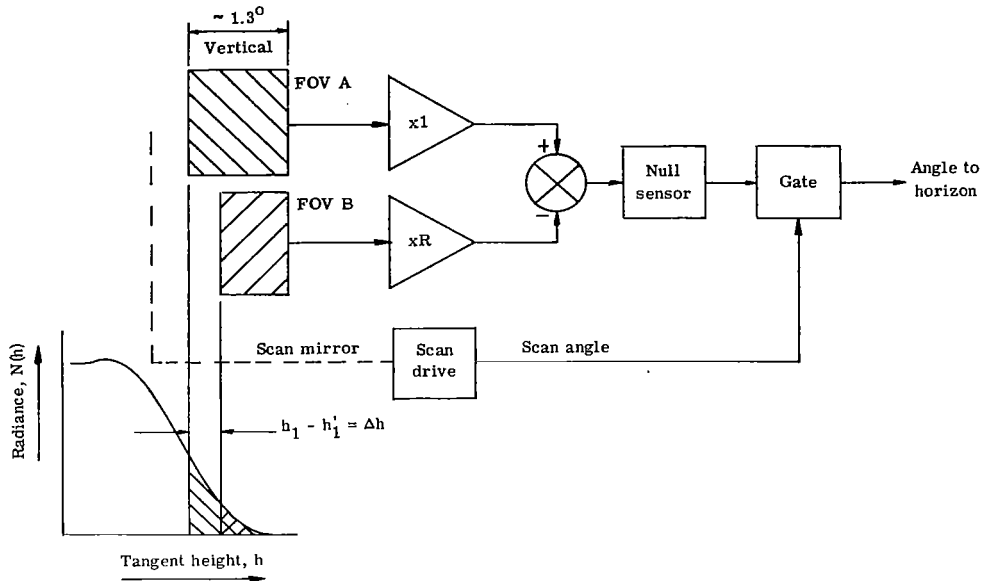


Figure 12.- Schematic representation of horizon sensor.

The outputs of the channels are subtracted, and when the difference voltage changes sign, the horizon is located. When the null is sensed, the instantaneous scan angle from the scan-angle readout subsystem is gated to provide the "located" horizon angle output.

Optical Subsystem

In each sensor head, the scan is generated by a mechanically resonant optical scanner. In this device, the flexure-pivot delivers the restoring force for the oscillating scan mirror, with the frequency of oscillation determined by the moment of inertia of the moving parts and the elastic constant of the flexure. Conventional bearings and their lubrication problems are avoided, and the small magnetic drive coils which start and maintain the oscillations consume very little power (typically less than 10 mW). If the scan mirror is placed in front of the sensor telescope, its size will be prohibitively large for use with a resonant optical scanner. This problem is circumvented when the mirror is placed in the convergent energy beam between the telescope objective and the focal plane, as shown in figure 13.

The sensor telescope uses a spherical objective mirror (1) which is 10 cm in diameter and has a 30.5-cm focal length. The folding mirror (2) serves as the aperture stop of the telescope and thus determines the clear aperture. The effective diameter of the optics is 6.14 cm. This design allows the telescope to focus off-axis energy with

- 1 Spherical objective mirror
- 2 Newtonian folding mirror
- 3 Optical scanner mirror
- 4 Band-pass filter, 14.0 to 16.3 μm
- 5 Field stop
- 6 Field lens - detector
- 7 Slit-shaped source
- 8 Beam splitter
- 9 Folding mirror
- 10 Collimating lens
- 11 Silicon detector array
- 12 Sun sensor

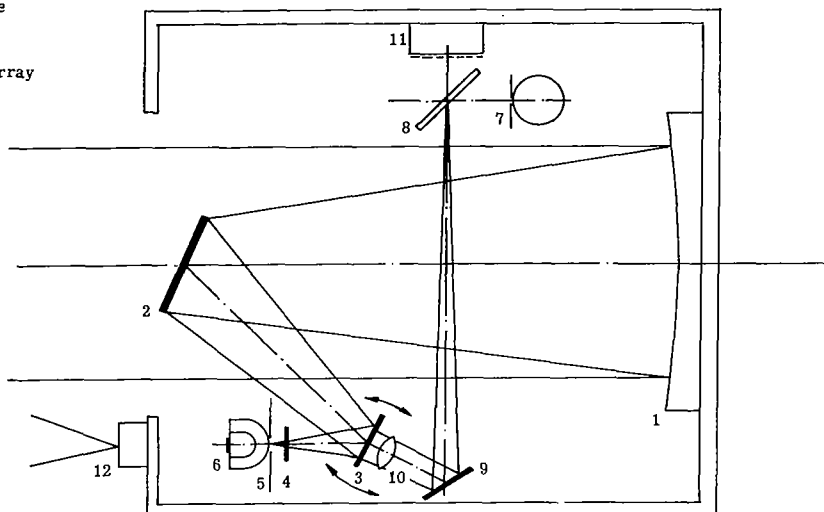


Figure 13.- Infrared horizon-sensor head.

acceptable aberrations. A computer ray trace was performed on this optical system. The blur-circle sizes in terms of kilometers at the horizon for a 500-km orbit as a function of the angle the incoming energy makes with the sensor axis are shown in table VI. These data compare with a blur circle of about 1-km diameter at the horizon due to diffraction.

TABLE VI.- DIAMETER OF OPTICAL BLUR CIRCLE

Energy in blur circle, percent	Blur-circle diameter, km, for off-axis angle of -			
	0° (a)	1°	2°	3°
68	0.16	0.32	0.68	1.14
90	.26	.53	1.08	1.87

^a On axis.

Bolometer Detector Subsystem

The detector subsystem consists of three immersed thermistor bolometers located side by side in the horizontal plane as shown in figure 14. Field of view B has been divided into two equal parts, which are located on opposite sides of field of view A. This division results in more nearly square detector flakes; in addition, small nonuniformities which may exist in the horizontal direction are smoothed out; also, the sensor head will

be less sensitive to skewing of the scan from the vertical. The combined width of the outside detectors is 4.65 times that of the center detector; thus, channel B has 4.65 times the gain of channel A.

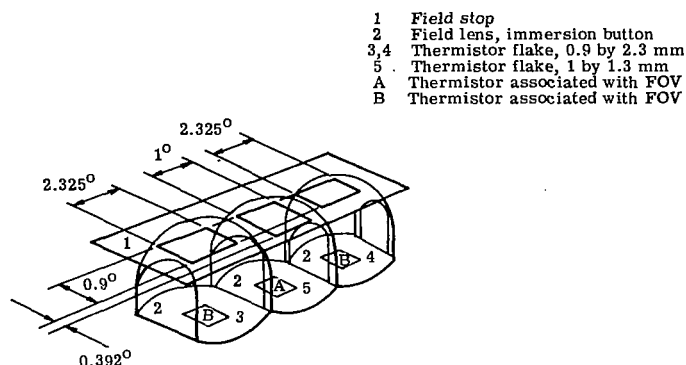


Figure 14.- Field stop and detector geometry.

The detector flakes are hyperimmersed in germanium so that the immersion lenses provide a magnification of 5.3. The center detector element (detector A) is 1 by 1.292 mm, and each outside flake (detector B) is 0.9 by 2.325 mm.

The field stop is located immediately in front of the immersion buttons and is dimensioned to have field of view A lead field of view B by the optimum separation distance of 17 km. The immersion lenses act as field lenses: They reimage the telescope aperture on the detector flake. This configuration has the advantage that nonuniformities across the detector surfaces are not projected to the image plane (the horizon). These radiation gradients might lead to errors in locating the horizon. The detectors are connected in a bridge circuit, as shown in figure 15. This circuit performs the subtraction of channel B from channel A; thus, all logic required by the locator is built into the detector subsystem to simplify the sensor and to increase reliability.

The flats on the immersion buttons are placed in intimate thermal contact; in this way compensation of the bridge for changes in ambient temperature is accomplished without the need for separate compensating flakes. These compensating flakes are customarily employed in bolometer detectors to balance out changes in detector responsivity and dc-offset voltage as a function of ambient temperature. The bridge circuit arrangement combined with the locator insensitivity to equal gain changes in each channel makes this possible, since only the ratio of the channel outputs is used. Removal of the compensating flakes results in increased detector responsivity and detectivity.

In infrared detector applications, the input radiation can be modulated by a chopper to reduce the excess (1/f) noise exhibited by these detectors. The present horizon locator does not allow the use of a chopper. At the required scan speed of 1 Hz and the limited chopping speed allowed by the relatively slow bolometer, the field of view would move a

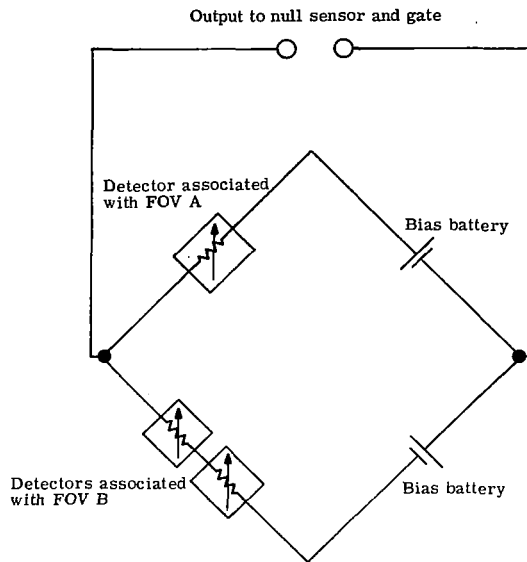


Figure 15.- Detector bridge circuit.

distance several times the size of a resolution element during each chopper off cycle, and therefore sensor accuracy would be limited. For this reason, the sensor will not contain a chopper; the attendant increase of $1/f$ detector noise must be accepted.

Sensor System Frequency Response

The resolution requirement is 1.5 km at the horizon (equivalent to 0.033° of arc motion of the fields of view), and the maximum scan rate is $15^\circ/\text{sec}$ (5° scanning oscillation at a rate of 1 Hz). They determine the time to sweep a resolution element as $t_s = \frac{0.033}{15} = 2.2 \text{ msec}$. To allow the detector to dwell two time constants on each resolution element, the detector time constant must be made one-half of t_s , or $\tau_{\text{det}} = 1.1 \text{ msec}$. The electronics upper frequency breakpoint required to match this response must be $f_h = \frac{1}{2\pi\tau_{\text{det}}} = 144 \text{ Hz}$. The total system will then exhibit a double upper frequency breakpoint at 144 Hz – one associated with the detector, the other with the electronics. The location of the low-frequency breakpoint of the electronics is determined from the following requirements. At the point where the horizon is located, the lower edge of the leading field of view (detector A) will point at about 25 km tangent height. (See table II.) Also, the detector starts to receive signal when, during its sweep from space to earth, its leading edge passes through approximately 65 km altitude. To operate as an integrator, the detector must retain all signals it receives while its edge moves from 65 to 25 km. The error caused by "droop" of the signal, that is, the amount the signal decreases because of the non-dc response of the system, is minimized by two effects. First, the signals that droop most are the low-amplitude signals associated with the highest tangent heights; also, the outputs of fields of view A and B decrease in approximately the same manner so that their ratio is affected less than with each individual channel.

A simulation study was performed (ref. 14) in which an analog computer was used to determine the optimum location of the low-frequency breakpoint and to evaluate effects of system frequency response on the accuracy of the sensor. The results of this study are presented in figure 16. Curve 1 is a computer-generated straight-line approximation

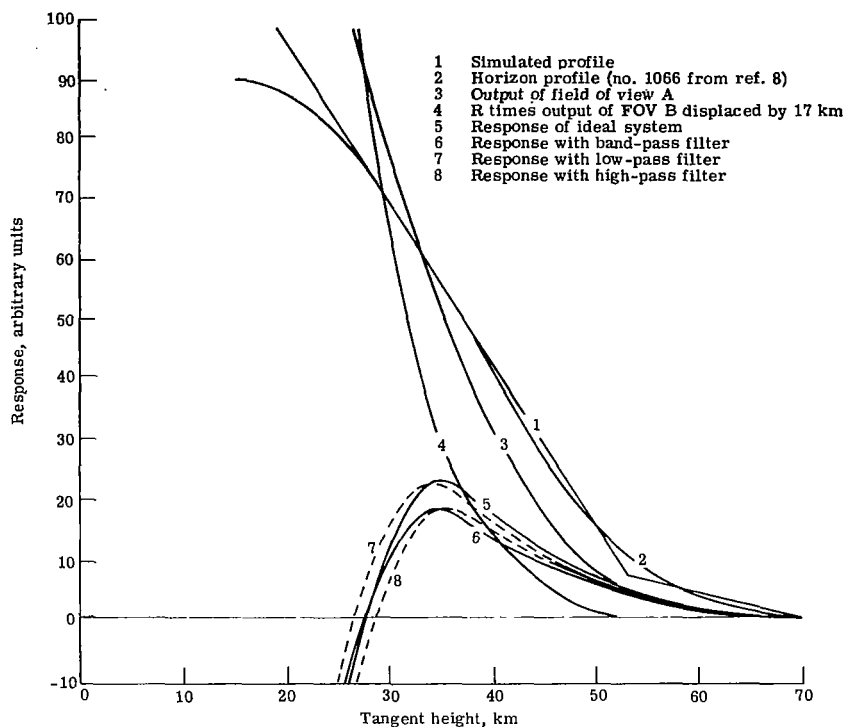


Figure 16.- System response.

of a representative horizon profile (curve 2). The approximated profile was convolved with two integrating fields of view whose leading edges were separated by 17 km. Additionally, the output of the lagging field of view was multiplied by gain factor $R = 4.65$. The resulting channel outputs are represented by curves 3 and 4. The two signals were subsequently passed through a simulated system filter and subtracted from one another. The lower and upper frequency breakpoint of the filter could be selected at any desired frequency. The resulting sensor output curves are shown by curves 5 to 8. Curve 5 shows the output of an "ideal" system, which has a flat response from dc to infinity; while curve 6 represents the output of the system with lower and upper frequency breakpoints at 2.5 and 144 Hz, respectively. The horizon is located at practically the same tangent height in both cases. This desirable result is caused by the interaction of the lower and upper frequency breakpoint effects. This interaction is illustrated by curves 7 and 8, which show that the upper frequency breakpoint at 144 Hz delays the zero-output crossing by about 2 km, whereas the droop caused by the 2.5-Hz lower frequency breakpoint moves the zero crossing in the opposite direction by an equal amount.

System Sensitivity

The sensor noise equivalent radiance NER can now be determined. As discussed previously, FOV A uses a hyperimmersed thermistor bolometer with a 1- by 1.3-mm flake size and a 1.1-msec time constant. This detector can be expected to have a detectivity D^* of $2 \times 10^8 \text{ cm-Hz}^{1/2}/\text{W}$ in the bandwidth between 2.5 and 144 Hz. When the detector is operated without a compensating flake, its effective D^* will be improved to $2.8 \times 10^8 \text{ cm-Hz}^{1/2}/\text{W}$. Furthermore, the equivalent noise bandwidth Δf of a system is defined as (ref. 15)

$$\Delta f = \frac{1}{K^2} \int_0^\infty |G(j\omega)|^2 df$$

where $G(j\omega)$ is the system transfer function and K is the midband gain of $G(j\omega)$. For the sensor system, which has a double frequency breakpoint located at 144 Hz, $\Delta f = 1.05(144) = 151 \text{ Hz}$. The noise equivalent radiance of FOV A can now be determined from the relation

$$NER = \frac{4\sqrt{\Delta f} f /}{\pi D^* \sqrt{\Delta \Omega} D \delta_{o,e}}$$

where

$f/$ f-number of the sensor telescope, $f/ = 5$

Δf noise equivalent bandwidth of electronics, $\Delta f = 151 \text{ Hz}$

D^* detector detectivity, $D^* = 2.8 \times 10^8 \text{ cm-Hz}^{1/2}/\text{W}$

$\Delta \Omega$ sensor solid field of view, $\Delta \Omega = 1.0^\circ \times 1.3^\circ = 4 \times 10^{-4} \text{ sr}$

D effective diameter of aperture of telescope, $D = 6.14 \text{ cm}$

$\delta_{o,e}$ efficiency of the optics and electronics, $\delta_{o,e} = 0.46$ (value assumed for an unchopped system)

The equation solved for these system parameters yields an NER of $0.05 \text{ W/m}^2\text{-sr}$. This amount of instrument noise was shown to introduce little error compared with inherent horizon variability. (See table III.)

Scan-Mirror Angle Readout

The scan-mirror angle readout indicates the direction to the located horizon with respect to the spacecraft. The digital mirror angle readout subsystem is shown in

figure 13. The output of a slit-shaped light source (7) is collimated and then reflected off the back surface of the scan mirror (3). The reflected light beam is then reimaged on an array of silicon photodetectors (11).

To read out the total scan angle of 5° with a resolution of 0.033° (1.5 km at the horizon for a 500-km orbit), 151 individual readout positions are needed. To reduce the number of elemental detectors needed, the back surface of the scan mirror is provided with two small reflecting flats mounted at 2.5° with respect to one another in the vertical direction; in this manner, the reflected light beam repeats itself two times per scan, and $\frac{151}{2} = 76$ elemental detectors are needed. To avoid ambiguity that can result from using two reflecting flats, electronic circuitry is used to identify which portion of the scan is active.

Arrayed silicon photodetectors are available with elemental detector center-to-center spacings of 0.015 cm. To match this spacing with the desired 0.033° readout resolution, the array must be located 26.5 cm from the scan mirror. This relatively long optical lever can be conveniently obtained by folding the beam as shown in figure 13. The overall length of the array must be 1.16 cm to enable readout of the total 5° scan angle.

Sun Presence Detection Subsystem

If the sun enters the horizon-sensor field of view, which could happen from time to time during a typical space flight application, erroneous attitude signals could be generated. In contrast, solar radiation which reaches the sensor after it is reflected by the earth and the atmosphere does not affect normal sensor operation, since in the 14- to 16- μm spectral interval this energy is negligible compared with that of the horizon signal. To provide a warning signal when the sensor looks directly at the sun, a "sun presence" detection system is used.

The sun sensor is a separate device which is attached to and boresighted with the horizon sensor head telescope. It consists of a small-diameter, simple lens with an unfiltered photodetector at the focal point. The field of view of this device is a solid angle of 10° so that when the sun approaches to within 5° of the horizon sensor optical axis a sun presence warning signal is generated. The spectral response of the sun sensor peaks at 0.9 μm spectral wavelength. The energy output of the sun within the detector spectral band pass is large; therefore, the detector can be a rather insensitive one.

CONCLUSIONS

A study was performed on a horizon locator concept which detects the earth's infrared CO_2 horizon at a relatively stable height regardless of atmospheric variations.

A digital computer simulation study was used to optimize sensor system parameters for maximum stability of the locator. The simulation study used 462 distinct synthesized radiance profiles, which represented a wide range of synoptic conditions and seasonal variability.

This set of profiles was also used to determine the sensitivity of the locator to a number of error sources, including changes in the horizon itself, as well as uncertainties in mission and horizon-sensor parameters. A simple and potentially reliable horizon sensor instrument which incorporates the present locator has been designed and analyzed.

The standard deviation (1σ) in located horizon altitude caused by phenomenological horizon noise alone was shown to be 0.798 km. This error increased to 1.14 km (1σ) when all noise sources considered were included. A conceptual design for a horizon sensor instrument which uses a compact optical system, immersed bolometer detectors, and simple electronic circuitry was presented.

Langley Research Center,
National Aeronautics and Space Administration,
Hampton, Va., December 22, 1971.

REFERENCES

1. Dodgen, J. A.; McKee, T. B.; and Jalink, A.: NASA - LRC Program To Define Experimentally the Earth's IR Horizon. Proceedings of the Second Symposium on Infrared Sensors for Spacecraft Guidance & Control, Barnes Engineering Co., c.1968, pp. 113-129.
2. McKee, Thomas B.; Whitman, Ruth I.; and Davis, Richard E.: Infrared Horizon Profiles for Summer Conditions From Project Scanner. NASA TN D-4741, 1968.
3. Whitman, Ruth I.; McKee, Thomas B.; and Davis, Richard E.: Infrared Horizon Profiles for Winter Conditions From Project Scanner. NASA TN D-4905, 1968.
4. Earle, M. D.: Infrared Horizon Sensor Accuracy in the Atmospheric Absorption Bands. Rep. No. TOR-269(4540-80)-3 (Contract No. AF 04(695)-269), Aerosp. Corp., June 1964. (Available from DDC as AD 460 971.)
5. Schwarz, Frank; Ward, Kenneth A.; and Falk, Thomas: A High-Accuracy Conical Scan Horizon Sensor Operating in the 15μ CO₂ Band. Proceedings of the First Symposium on Infrared Sensors for Spacecraft Guidance & Control, Barnes Engineering Co., c.1965, pp. 75-88.
6. Thomas, John R.: Derivation and Statistical Comparison of Various Analytical Techniques Which Define the Location of Reference Horizons in the Earth's Horizon Radiance Profile. NASA CR-726, 1967.
7. Bates, Jerry; Hanson, David S.; House, Fred B.; Carpenter, Robert O'B.; and Gille, John C.: The Synthesis of 15μ Infrared Horizon Radiance Profiles From Meteorological Data Inputs. NASA CR-724, 1967.
8. Anon.: Compilation of Atmospheric Profiles and Synthesized 15μ Infrared Horizon Radiance Profiles Covering the Northern Hemisphere in the Longitude Region Between 60° W and 160° W From March 1964 Through February 1965. Pts. I and II. NASA Contract NAS 1-6010, Honeywell, Inc., Oct. 1966. (Available as NASA CR-66184 and NASA CR-66185.)
9. Peterson, Roy E.; Schuetz, John; Shenk, William E.; and Tang, Wen: Derivation of a Meteorological Body of Data Covering the Northern Hemisphere in the Longitude Region Between 60° W and 160° W From March 1964 Through February 1965. NASA CR-723, 1967.
10. Thomas, John R.; Jones, Ennis E.; Carpenter, Robert O'B.; and Ohring, George: The Analysis of 15μ Infrared Horizon Radiance Profile Variations Over a Range of Meteorological, Geographical, and Seasonal Conditions. NASA CR-725, 1967.

11. Anon.: U.S. Standard Atmosphere, 1962. NASA, U.S. Air Force, and U.S. Weather Bur., Dec. 1962.
12. Thomas, John R.; Carson, John C.; Williamson, William R.; Florant, Lester B.; Grienel, Herman P.; and Hoffman, Allan D.: Attitude-Referenced Radiometer Study. Vol. II - Precision Radiometric System. NASA Contract No. NAS 1-8801, Honeywell, Inc., Aug. 1969. (Available as NASA CR-66855.)
13. Anon.: Scout Planning Guide. Missiles and Space Div., LTV Aerospace Corp., Oct. 1968.
14. Johnson, Clarence L.: Analog Computer Techniques. Second ed., McGraw-Hill Book Co., Inc., c.1963.
15. Schwartz, Mischa: Information Transmission, Modulation, and Noise. McGraw-Hill Book Co., Inc., 1959.